Nano-Micro Letters

ISSN 2311-6706
e-ISSN 2150-5551
CN 31-2103/TB

ARTICLE

https://doi.org/10.1007/s40820-021-00690-8

Cite as
Nano-Micro Lett.
(2021) 13:172

Received: 22 April 2021
Accepted: 24 June 2021
Published online: 12 August 2021

Water-Dispersible $CsPbBr_3$ Perovskite Nanocrystals with Ultra-Stability and its Application in Electrochemical CO_2 Reduction

Keqiang Chen[1,2], Kun Qi[1], Tong Zhou[3], Tingqiang Yang[1], Yupeng Zhang[1] ✉, Zhinan Guo[1], Chang-Keun Lim[2,4], Jiayong Zhang[5], Igor Žutic [3], Han Zhang[1] ✉, Paras N. Prasad[2] ✉

HIGHLIGHTS

- Water-dispersible $CsPbBr_3$ nanocrystals (NCs) exhibit ultra-stability (>200 days) in water with only ~20% decline of the initial photoluminescence intensity.
- The as-prepared ultra-stable water-dispersible $CsPbBr_3$ NCs showed high electrocatalysis activity (faradaic yield: 32% for CH_4, 40% for CO) and operation stability (>350 h) for CO_2 reduction reaction.

ABSTRACT Thanks to the excellent optoelectronic properties, lead halide perovskites (LHPs) have been widely employed in high-performance optoelectronic devices such as solar cells and light-emitting diodes. However, overcoming their poor stability against water has been one of the biggest challenges for most applications. Herein, we report a novel hot-injection method in a Pb-poor environment combined with a well-designed purification process to synthesize water-dispersible $CsPbBr_3$ nanocrystals (NCs). The as-prepared NCs sustain their superior photoluminescence (91% quantum yield in water) for more than 200 days in an aqueous environment, which is attributed to a passivation effect induced by excess CsBr salts. Thanks to the ultra-stability of these LHP NCs, for the first time, we report a new application of LHP NCs, in which they are applied to electrocatalysis of CO_2 reduction reaction. Noticeably, they show significant electrocatalytic activity (faradaic yield: 32% for CH_4, 40% for CO) and operation stability (> 350 h).

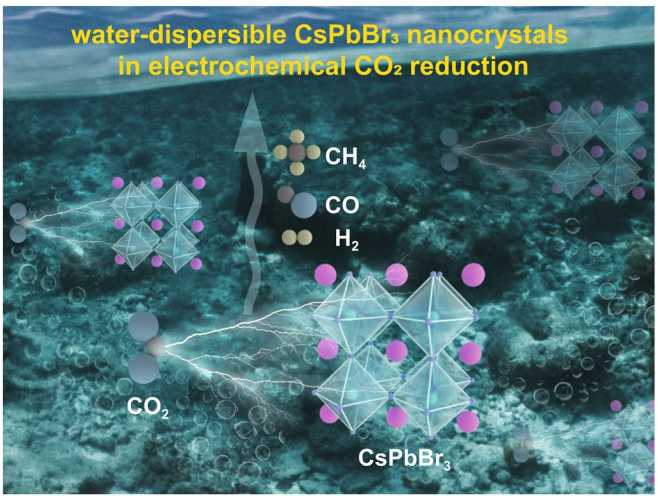

KEYWORDS $CsPbBr_3$ nanocrystals; Water-dispersible; Ultra-stability; Electrochemical CO_2 reduction

Keqiang Chen, Kun Qi, Tong Zhou, and Tingqiang Yang contributed equally to this work.
✉ Yupeng Zhang, ypzhang@szu.edu.cn; Han Zhang, hzhang@szu.edu.cn; Paras N. Prasad, pnprasad@buffalo.edu
[1] Key Laboratory of Optoelectronic Devices and Systems of Ministry of Education and Guangdong Province, Institute of Microscale Optoelectronics, Shenzhen University, Shenzhen 518060, People's Republic of China
[2] Institute for Lasers, Photonics, and Biophotonics, Department of Chemistry, University at Buffalo, State University of New York , Buffalo, NY 14260, USA
[3] Department of Physics, University at Buffalo, State University of New York, Buffalo, NY 14260, USA
[4] Department of Chemical and Materials Engineering, School of Engineering, Nazarbayev University, Nur-Sultan City 010000, Kazakhstan
[5] Jiangsu Key Laboratory of Micro and Nano Heat Fluid Flow Technology and Energy Application, School of Physical Science and Technology, Suzhou University of Science and Technology, Suzhou, Jiangsu 215009, People's Republic of China

1 Introduction

Electrochemical or photochemical reduction of carbon dioxide (CO_2) could efficiently recycle the greenhouse gas back to fuels [1–3]. However, the existing perovskite catalysts are either inefficient or unstable. In addition, a weak binding interaction between the catalyst and the intermediates gives rise to high overpotential or slows the electron transfer kinetics, finally resulting in low-exchange current densities and turnover frequencies [4]. Both of these metrics depend on the intrinsic electronic properties of the catalyst, and also on the size effect, for example, bulk vs. nanostructures, thus current research hotspots are single-atom catalysts and also nanocrystals (NCs) catalysts [5, 6]. The emergence of lead halide perovskites (LHPs) substantially accelerates the development of material science [7–9]. Their outstanding optoelectronic properties, such as high photoluminescence (PL) quantum yield (PLQY), exceptional defect tolerance, long carrier diffusion lengths, lead to their wide applications in high-performance optoelectronic devices and photocatalysts [10–19]. However, the ionic nature of LHPs lead to their fast decomposition in the presence of water or moisture [20–22]. As a result, noticeable degeneration of the performance of LHP-based devices might arise when exposed to ambient condition [23]. Their poor stability against water largely restricts their applications in aqueous systems, such as electrocatalysis and biomedical labeling. Searching for a suitable strategy to synthesize water-stable or even water-dispersible LHPs is of significance to enhance the stability of LHP-based devices, as well as widen the field of LHP applications.

Till now, substantial efforts have been carried out to synthesize water-dispersible and -stable LHPs [24–31]. Especially, Wu et al. [28] obtained $CsPbX_3$ NCs through a water-triggered phase transformation of Cs_4PbX_6 NCs. Interestingly, these $CsPbX_3$ NCs exhibit improved stability against moisture due to the surface passivation effect. However, the as-prepared $CsPbX_3$ NCs are still hexane-dispersible. Making core–shell structure is an effective approach to reduce the defects on the core surface and protect the core structure. Zhong et al. [32] reported a novel one-pot method for the synthesis of $CsPbBr_3$@SiO_2 core–shell nanostructure, which can greatly enhance the water-stability of $CsPbBr_3$. Li et al. [33] synthesized $CsPbBr_3$/polymer core–shell structure, which can reduce nonradiative current losses and improve quantum efficiency. However, these shell layers are almost insulating, which would result in poor charge transfer efficiency and reduce the performances of various devices. Li et al. [34] prepared $CsPbBr_3/TiO_2$ core–shell structure through the hydrolyzation of titanium butoxide (TBOT), more importantly, the TiO_2 shell layer promotes enhanced water-stability and charge separation efficiency. However, the as-synthesized $CsPbBr_3/TiO_2$ core–shell structure possesses poor dispersibility in water. Recently, several publications reported that water-stable LHP NCs can be obtained through Lewis base vapor diffusion (LBVD) [35–37], aqueous synthesis protocol [30], or aqueous phase exfoliation methods [38]. However, their water-dispersibility or -stability is still not ideal for practical applications in an aqueous system. Moreover, the limited water stability of LHP leads to a largely overlooked application in electrocatalysis.

In this contribution, water-dispersible $CsPbBr_3$ NCs were produced using a novel hot-injection method in a Pb-poor environment combined with a well-designed purification process. For the first time, $CsPbBr_3$ NCs with good water dispersibility and excellent water stability (> 200 days) were realized. The water-dispersible $CsPbBr_3$ NCs exhibit a high PLQY of 91%, which is much better than that of $CsPbBr_3$ NCs dispersed in hexane (79%). Density-functional theory (DFT) calculation elucidates the ultra-stability of the water-dispersible $CsPbBr_3$ NCs should be owned to the CsBr salt-rich environment, which reduces the surface defect density and prevents the structural degradation induced by water. Finally, the water-dispersible $CsPbBr_3$ NCs were applied to the electrocatalysis of the CO_2 reduction reaction (RR) in an aqueous system, resulting in high faradaic yields to CH_4 (32%) and CO (40%).

2 Experimental Section

2.1 Chemicals

Lead bromide ($PbBr_2$, 99.999% trace metals basis), cesium acetate (CsOAc, $C_2H_3CsO_2$, 99.9% trace metals basis), zinc bromide ($ZnBr_2$, 99.999% trace metals basis),

https://doi.org/10.1007/s40820-021-00690-8

1-octadecene (ODE, $C_{18}H_{36}$, technical grade, 90%), oleylamine (OLA, $C_{18}H_{37}N$, technical grade, 70%), oleic acid (OA, $C_{18}H_{34}O_2$, technical grade, 90%), and hexane (C_6H_{14}, 98%) were purchased from Sigma Aldrich. All chemicals were used without any further purification.

2.2 Preparation of Cs-OA Solution

0.192 g (1 mmol) CsOAc and 2 mL OA were mixed in a flask, and the mixture was heated to 120 °C under atmosphere until all CsOAc was dissolved.

2.3 Synthesis and Purification of Water-dispersible $CsPbBr_3$ Nanocrystals

The water-dispersible $CsPbBr_3$ nanocrystals were synthesized under a Cs- and Br-rich, which is a Pb-poor, environment. Briefly, 0.05 mmol $PbBr_2$ and 0.95 mmol $ZnBr_2$, which were used as Pb and Br sources (here, the $ZnBr_2$ was used as the Br-source, which can provide a Br-rich environment, and Zn will not enter into the crystal lattice) [39, 40], were added into a 50 mL three-nicked flask that contained 20 mL ODE. The mixture was stirred and heated to 120 °C in an Ar atmosphere. 3 mL OA and OLA were used as surface ligands and added into the above solution. The temperature was raised to 180 °C after the complete dissolution of $PbBr_2$ and $ZnBr_2$, and then, 1 mL Cs-OA solution was swiftly injected. The reaction solution was cooled down to room temperature after 5 s reaction. The crude solution was directly centrifuged at 9000 rpm for 10 min. The suspension was discarded, and the precipitate was re-dispersed in 10 mL hexane. Subsequently, another centrifugation process was carried out at 9000 rpm for 10 min, the suspension and the precipitate (nonluminescent) were mixed separately with 2 mL of water under sonication, which resulted in $CsPbBr_3$ nanocrystals with completely opposite dispersibility in hexane(marked as h-$CsPbBr_3$) or water (marked as w-$CsPbBr_3$), respectively. More detailed information can be found in Fig. S1.

2.4 Electrode Preparation Process

The electrode was prepared by the spin-coating process described as following: $CsPbBr_3$ NCs (w-$CsPbBr_3$, without centrifugation process) thin film electrode was fabricated via spin-coating process. Before spin-coating, substrates were cleaned via ultrasonication in pure water, and after drying them, their surface was treated using a UV ozone cleaner (UV253E, Filgen) to decompose surface contaminants. For the electrochemical measurement, the edge and backside of the glassy carbon electrode were masked with caption tape to avoid the hydrogen evolution reaction. For spin-coating, the suitable concentration of $CsPbBr_3$ NCs-5% Nafion solution ink was drop casted on the surface of the electrode. Spin-coating was conducted at 3000 rpm for 10 s and repeated 20 times until the loading amount reached 0.3 mg cm^{-2}.

2.5 CO_2 RR Testing

The electrochemical measurements were performed using a Biologic SP-300 potentiostat. Ambient pressure CO_2 electrolysis was carried out in a custom-made gas-tight electrochemical cell made of poly-carbonate and fitted with Buna-N O-rings built in our laboratory. The configuration of the electrochemical cell is such that the working electrode sits parallel with respect to the counter electrode to ensure a uniform potential distribution across the surface. The geometric surface area for both of the electrodes is 1.4 cm^2. A Nafion 117 proton exchange membrane is used to separate the anodic and the cathodic compartments. Each of the compartments in this cell contains a small volume of electrolyte (2 mL each) to concentrate liquid products and therefore increase the detection limits. 0.1 M $KHCO_3$ solution was used as the electrolyte, which was prepared by 1 h CO_2 bubbling into 0.05 M K_2CO_3 solution (purified with Chelex resin to eliminate metallic impurities). Before starting the CO_2 electrolysis, the electrolyte in the cathodic compartments was purged with CO_2 for at least 15 min. During electrolysis, CO_2 was constantly bubbled through the electrolyte at a flow rate of 5 sccm to prevent depletion of CO_2 in the electrolyte and to allow the continuous analysis of gaseous products via a gas chromatograph. The flow rate of CO_2 was controlled with a mass flow controller (Bronkhorst), and the gas was first humidified with water by passing it through a bubbler to minimize evaporation of the electrolyte. A platinum foil was used as the counter electrode, and an Ag/AgCl electrode (leak-free series) from Innovative Instruments, Inc. was used as the reference. Voltages were converted to the RHE scale by using a calibrated reference electrode as in the equation below:

$$E(\mathrm{RHE}) = \mathrm{EAg/AgCl} + 0.0591 * \mathrm{pH} + E^{0}\mathrm{Ag/AgCl}$$

2.6 Product Analysis

For the analysis of gaseous products, a gas chromatograph (GC, SRI instruments) equipped with a HayeSep D porous polymer column, thermal conductivity detector, and flame ionization detector, was used. Ultra-high purity Ar (99.999%) was used as the carrier gas. The concentrations of gaseous products were determined using calibration curves from standard gas mixtures. During electrolysis, CO_2 was constantly bubbled through the electrolyte to prevent depletion of CO_2 in the electrolyte, and to allow continuous analysis of gaseous products via the GC.

2.7 Characterization

The crystal structures and microstructures of the as-synthesized samples were examined using XRD with Cu Kα radiation (Bruker D8 Advance powder X-ray diffractometer) and TEM (JEM-3100, JEOL, Japan). The optical properties of the as-synthesized samples were determined using a UV − vis spectrophotometer (UV − 3101PC, Shimadzu) with excitation provided by a 365 nm laser (RF-5301PC, Shimadzu) using $CsPbBr_3$ NCs solutions. h-$CsPbBr_3$ and w-$CsPbBr_3$ NCs were separately kept in two sealed quartz cuvettes for the water-stability testing. In order to minimize the errors, the same positions of each quartz cuvettes were used during the testing. The PLQY was examined with a Hamamatsu C11347-12 Quantaurus-QY fluorescence spectrometer using $CsPbBr_3$ NCs solutions. The blank solutions (*i.e.,* hexane and water for h-$CsPbBr_3$ and w-$CsPbBr_3$ NCs, respectively) were measured and named as references, then the PLQY of h-$CsPbBr_3$ and w-$CsPbBr_3$ NCs were received by deducting the references. The time-resolved PL lifetime was collected with a fluorescence spectrometer (FLS 980) using a 507 nm laser for excitation (EPL-510, Edinburgh Instruments Ltd) using $CsPbBr_3$ NCs solutions. ζ potential data was collected using a Zetasizer Nano ZSE analyzer (Malvern, United Kingdom).

2.8 Density-Functional Modeling Methods

The geometry optimization and electronic structure calculations were performed by using the projector augmented wave method (PAW) [41] based on the density-functional theory (DFT), as implemented in the Vienna ab initio simulation package (VASP) [42]. The Perdew-Burke-Ernzerhof generalized-gradient approximation (PBE- GGA) [43] is used to describe the exchange and correlation functional. All calculations were carried out with a plane-wave cutoff energy of 450 eV. For the calculation on the interaction between $CsPbBr_3$ NCs and water molecule, a periodic (1×1) surface supercell is built with a vacuum layer of 20 Å, and the Monkhorst–Pack k-point grids of $9\times9\times1$ are adopted for the first Brillouin zone integral. For the calculation on processes of CO_2 RR at $CsPbBr_3$ NCs, a periodic (2×2) surface supercell is built with a 20 Å vacuum layer, and Monkhorst–Pack k-point grids of $3\times3\times1$ are adopted. The final stable atomic structures are obtained through full relaxation with a total energy tolerance of 10^{-6} eV. The van der Waals interaction functional with the method of Grimme (DFT-D3) [44] was employed in the calculations.

3 Results and Discussion

3.1 Synthesis and Characterization of $CsPbBr_3$ NCs

The synthesis process was carried out in a Pb-poor and Cs-/Br-rich environment through a hot-injection method (more details can be found in Experimental Section). In a Cs-/Br-rich environment, the expected products should be a mixture of $CsBr/Cs_4PbBr_6$. The crude solution exhibited white color without any visible PL. A well-designed purifying process was carried out to obtain water-dispersible $CsPbX_3$ NCs from the crude solution, as shown in Fig. S1. The reaction solvents, including 1-octadecene (ODE), oleic acid (OA), and oleylamine (OLA), were separated from the crude solution by direct centrifugation. Then, a further centrifugation process was performed after re-dispersion of the precipitate in hexane. Both the suspension and the precipitate showed mixed phases of $CsBr/Cs_4PbBr_6$ (Fig. S2) without any PL. A phase transformation from Cs_4PbBr_6 to $CsPbBr_3$ was observed after inducing of water (Fig. 1), the $CsPbBr_3$ phase with strong PL emission emerged in both h-$CsPbBr_3$ (dispersed in hexane) and w-$CsPbBr_3$ (dispersed in water).

Surprisingly, these NCs exhibited completely opposite dispersibility in hexane or water, as shown in Fig. 2a. In the preparation process of w-$CsPbBr_3$, an organic layer emerged at the top of the water layer after sonication, which indicated

 https://doi.org/10.1007/s40820-021-00690-8

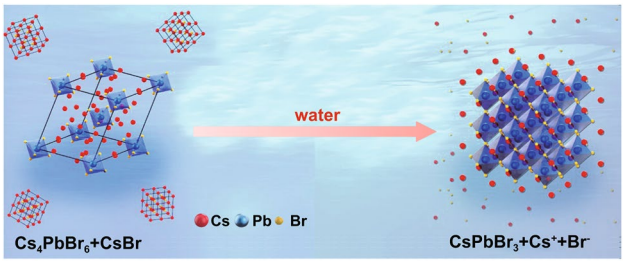

Fig. 1 Schematic of the phase transformation from $CsBr/Cs_4PbBr_6$ to $CsPbBr_3$

the removal of the surface organic ligands. Fourier transform infrared (FTIR) spectroscopy further confirmed that most of the ligands had been removed. As shown in Fig. S3, the vibrational bands around 3000 cm^{-1} (C–H stretching) and below 2000 cm^{-1} (C=O/C=C stretching and C-H banding) belonging to oleylammonium, oleate, or octadecene [45] are almost disappeared. XRD patterns (Fig. S2) clearly showed the pure $CsPbBr_3$ phase of h-$CsPbBr_3$, while w-$CsPbBr_3$ can be indexed as a mixture of CsBr and cubic $CsPbBr_3$ phases [46, 47]. Furthermore, the pure cubic $CsPbBr_3$ phase from w-$CsPbBr_3$ had also been obtained after centrifuging at 13,000 rpm for 20 min (Fig. 2b), indicating the perfect water solubility of CsBr in w-$CsPbBr_3$. Transmission electron microscopy (TEM) images of w-$CsPbBr_3$ (after centrifugation) and h-$CsPbBr_3$ NCs are shown in Figs. 2c and S4, both samples have uniform size distributions (19.49 and 8.77 nm for w-$CsPbBr_3$ and h-$CsPbBr_3$, respectively, Fig. S5), regular morphologies, and good crystallization. The interlattice distances of 0.292 and 0.419 nm matched well with the d-spacing of (200) and (110) crystal planes of cubic $CsPbBr_3$. The optical properties of h-$CsPbBr_3$ and w-$CsPbBr_3$ NCs were further studied by UV–vis absorption and PL spectra, as shown in Fig. 2d. The absorption onset and the PL peak of h-$CsPbBr_3$ NCs are determined at 519 and 514 nm, respectively, which are 2 nm lower than those of w-$CsPbBr_3$ NCs (521 and 516 nm). Interestingly, w-$CsPbBr_3$ NCs exhibited a narrower full width at half-maximum (FWHM) of 18 nm and a higher PLQY (91%) than those of h-$CsPbBr_3$ NCs (21 nm and 79%, respectively).

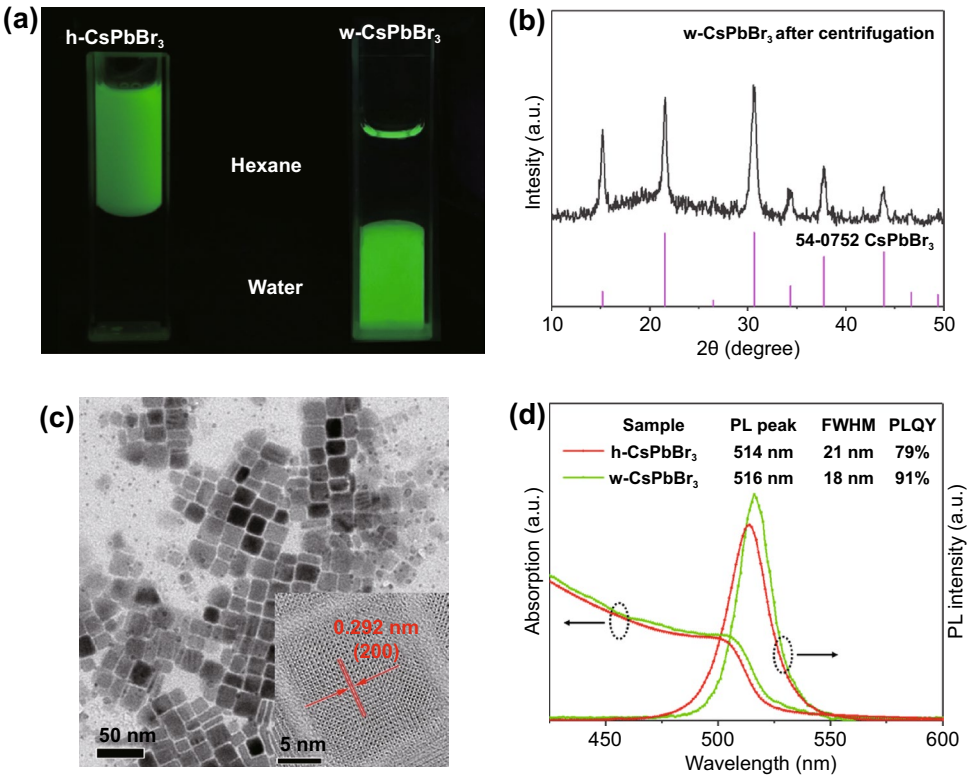

Fig. 2 **a** Photographs of h-$CsPbBr_3$ and w-$CsPbBr_3$ NCs under UV light; XRD pattern (**b**) and TEM image (**c**) of w-$CsPbBr_3$ NCs after centrifugation; **d** UV–vis absorption and PL spectra of w-$CsPbBr_3$ NCs

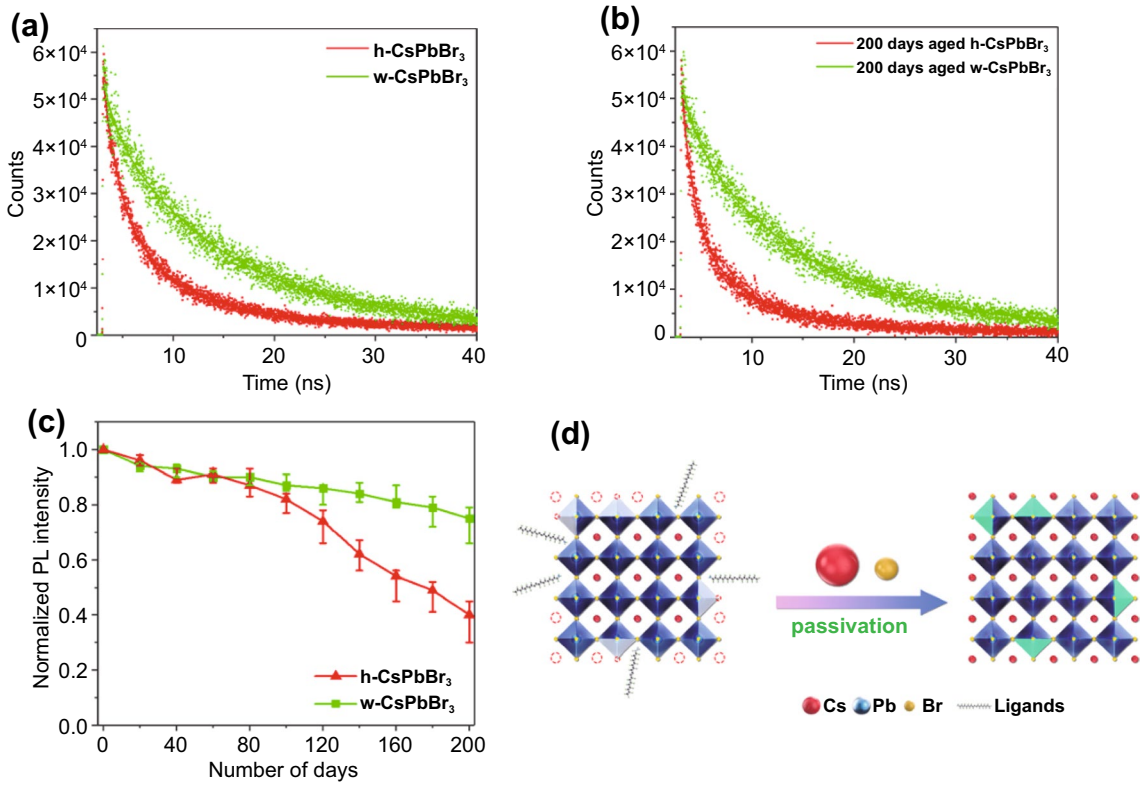

Fig. 3 TRPL spectra of freshly prepared (**a**) and 200 days aged (**b**) h-$CsPbBr_3$ and w-$CsPbBr_3$ NCs, respectively; **c** PL stabilities of h-$CsPbBr_3$ and w-$CsPbBr_3$ NCs; **d** schematic of the surface passivation of $CsPbBr_3$ NCs

The time-resolved PL (TRPL) shown in Fig. 3a indicated that w-$CsPbBr_3$ NCs has a longer PL lifetime (10.27 ns) than that of h-$CsPbBr_3$ NCs (4.49 ns), suggesting a lower surface defect density in w-$CsPbBr_3$ NCs, which is attributable to the surface passivation effect induced by the Cs^+ and Br^- ions in water [48]. In addition, the PL lifetime of 200 days aged w-$CsPbBr_3$ NCs was 9.90 ns (Fig. 3b), which is close to the initial value (10.27 ns). In contrast, a significant decrease in the PL lifetime from 4.49 ns (initial) to 2.92 ns (200 days aged) was observed for h-$CsPbBr_3$ NCs, which further revealed the lower surface defect density and improved stability of w-$CsPbBr_3$ NCs. Figure 3c demonstrated the PL stability of h-$CsPbBr_3$ and w-$CsPbBr_3$ NCs. Unexpectedly, w-$CsPbBr_3$ NCs received a better PL stability than that of h-$CsPbBr_3$ NCs. w-$CsPbBr_3$ NCs could maintain 80% of its initial PL intensity for more than 200 days. However, the PL intensity of h-$CsPbBr_3$ NCs decreased rather rapidly after 100 days, and could only preserve about 40% of its initial PL intensity after 200 days. Surprisingly, when the freshly prepared w-$CsPbBr_3$ NCs were centrifuged and re-dispersed in pure water, complete quenching of the PL emission was observed within 24 h. That is to say, the CsBr salt in water played a crucial role for the ultra-stability of w-$CsPbBr_3$ NCs. It is well known that the $CsPbX_3$ (X = Cl, Br, I) NCs are terminated by either CsX or PbX_2, and passivated by oleylammonium ions (OLA^+), which occupy the A-sites (h-$CsPbBr_3$) [49]. The loss of OLA^+ and the emergence of Br-vacancy would occur gradually over time (Fig. 3d), which leads to the degeneration of both the crystal structure and the optical properties. As the organic ligands on the surface of w-$CsPbBr_3$ NCs had been removed after the washing process, the sufficient Cs^+ and Br^- ions in the water can passivate the defects induced by the loss of OLA^+ and Br^- ions (Fig. 3d). Therefore, we believe that the CsBr salt in water is essential for the better performance of w-$CsPbBr_3$ NCs.

 https://doi.org/10.1007/s40820-021-00690-8

3.2 Water Stability Mechanism

Generally, the stability of material can be evaluated on the basis of the robustness of the crystal and electronic structures against environment. Specifically, if the crystal and electronic structures of one material remain unchanged when interacting with the environment, it can be regarded as a stable material under this environment. In contrast, the material is unstable. Changes in the crystal structure can be directly obtained from the structure distortion after structural relaxations, and changes in electronic structure are usually reflected in the charge redistributions (known as charge transfer). Such crystal structure distortion and charge redistributions have been widely used to check the stability of perovskites in a specific environment using DFT calculations [50–52]. Here, we calculated the crystal structure distortions and charge redistributions of the $CsPbBr_3$ after the adsorption of H_2O molecules to elucidate the mechanism of CsBr-induced water-stability of w-$CsPbBr_3$ NCs. It is well known that $CsPbBr_3$ possesses a $PbBr_2$ terminated surface (Fig. S6a, d) [43], the structure distortion of $[PbBr_6]^{4-}$ octahedra and octahedral cavities induced by the adsorption of a water molecule can be clearly observed, as shown in Figs. 4a and S7a. The deviations of the Pb – Br bond lengths and Pb – Br – Pb bond angles were listed in Table S1 and Fig. S7. Such structural distortions were also verified by calculating the charge distribution, which is described by the differential charge density of the system, $\Delta\rho = \rho(H_2O/CsPbBr_3) - \rho(H_2O) - \rho(CsPbBr_3)$, where $\rho(H_2O/CsPbBr_3)$, $\rho(H_2O)$, and $\rho(CsPbBr_3)$ are the charge densities of the $H_2O/CsPbBr_3$, H_2O, and $CsPbBr_3$, respectively. As shown in Fig. 4d, $\Delta\rho$ is mainly distributed in the first layer of the $[PbBr_6]^{4-}$ octahedra, indicating a noticeable structural distortion of the $[PbBr_6]^{4-}$ octahedra on the surface. Figure S6b, e demonstrate the $CsPbBr_3$ structure with a Br-vacancy, which is common due to the easy loss of Br^- ions. When one H_2O molecule is absorbed, distinct distortions can be observed both at the surface (first layer) and the inner structure (second layer), as shown in Figs. 4b and S5b. In this case, $\Delta\rho$ not only existed in the first layer of $[PbBr_6]^{4-}$ octahedra, but also emerged in the second layer of $[PbBr_6]^{4-}$ octahedra, indicating that the water molecules

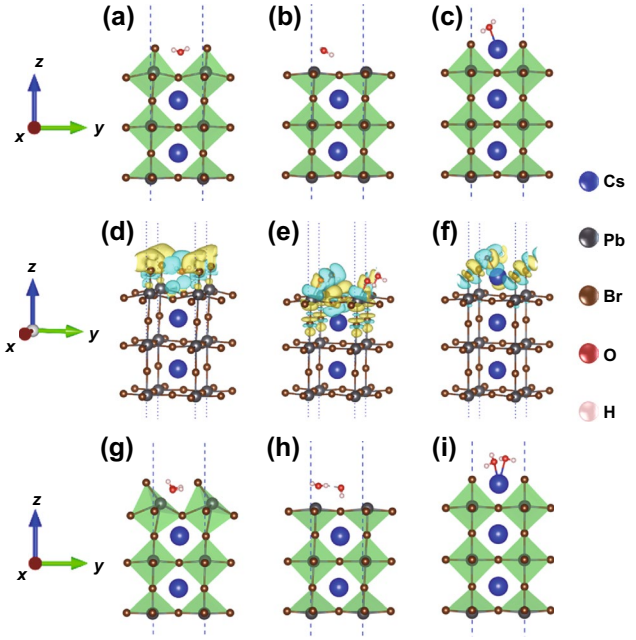

Fig. 4 Relaxed polyhedral models of $CsPbBr_3$ with (**a**) initial, **b** Br-vacancy, and (**c**) CsBr passivated structures after adsorption of one water molecule. **d–f** Diffrential charge density for (**a–c**), respectively. The yellow and cyan regions represent electron accumulations and depletions, respectively, where the isosurface value was set to 0.002 e $Å^{-3}$. Relaxed polyhedral models of $CsPbBr_3$ with (**g**) initial, (**h**) Br-vacancy, and (**i**) CsBr passivated structures after adsorbing two water molecules. Blue, gray, brown, red, and pink spheres represent Cs, Pb, Br, O, and H atoms, respectively

can even induce the distortion to the $[PbBr_6]^{4-}$ octahedra inside (Fig. 4e). The appearance of CsBr can lead to a CsBr terminated surface, which produced CsBr passivation, as shown in Fig. S6c, f. With such a CsBr passivated surface, the $[PbBr_6]^{4-}$ octahedra were more stable even after the adsorption of water molecules, as shown in the relaxed structural geometries (Figs. 4c and S7c), where the structural deviations were minimal (Table S1). As seen in Fig. 4f, the charge transfer only existed around the Cs atoms on the surface, indicating that the water molecules had little effect on the $[PbBr_6]^{4-}$ octahedra. The CsBr terminated surface can be seen as a protective shell for the $[PbBr_6]^{4-}$ octahedra structures. Subsequently, two water molecules were further introduced onto the surface of various structures (Figs. 4g-i and S7d-f). Interestingly, the distortion of the $PbBr_2$ terminated and Br-vacancy crystal lattice became more prominent

compared to the results shown in Fig. 4a, b. No significant difference can be found for the CsBr passivated structure after adsorbing two water molecules, suggesting that the CsBr passivated structure was very stable. These results further revealed that the CsBr salt plays a crucial role for the ultra-stability of w-$CsPbBr_3$ NCs in water.

In addition, we believe that the Cs^+ and Br^- ions in water can form an electrical double layer (EDL) on the surface of w-$CsPbBr_3$ NCs due to the large ζ potential (> 80 mV, Figs. S8 and S9) [53]. The stability of perovskite NCs in hexane highly relies on lipophilic ligands on the surface. In contrast, the high stability of w-$CsPbBr_3$ NCs against water in this work is attributed to EDL, which is extensively believed to be the reason for the good dispersibility of colloids in water. Both Cs_4PbBr_6 and $CsPbBr_3$ are composed of $[PbBr_6]^{4-}$ octahedrons and Cs^+ ions. For Cs_4PbBr_6, $[PbBr_6]^{4-}$ octahedrons are completely separated from each other and surrounded by Cs^+ ions, while the $[PbBr_6]^{4-}$ octahedrons in $CsPbBr_3$ share all corners with Cs^+ ions filling in voids [28]. Due to the high solubility of Cs^+ ions in water, Cs_4PbBr_6 and $CsPbBr_3$ NCs covered by lipophilic ligands show poor stability against moisture. The stability of Cs_4PbBr_6 is even worse than that of $CsPbBr_3$ because of its incompact structure, and Cs_4PbBr_6 can transform to $CsPbBr_3$ by stripping Cs^+ and Br^- ions into water [28]. In this work, once we disperse the CsBr/Cs_4PbBr_6 NCs into water and sonication, surface ligands can be removed. In addition, the CsBr NCs will immediately be dissolved, and Cs^+ ions will gradually leach from Cs_4PbBr_6 NCs and result in a negative charge of the remaining part of Cs_4PbBr_6, which in turn slows down the leaching of Cs^+ ions. Additionally, the Br^- also begins to leach into the water to maintain electric neutrality, and the isolated $[PbBr_6]^{4-}$ octahedrons will share their corners. The $[PbBr_6]^{4-}$ framework with Cs^+ ions filling into the voids is exactly the structure of $CsPbBr_3$. At this moment, the newly-formed $CsPbBr_3$ NCs are surrounded by high concentration Cs^+ and Br^- ions. Cs^+ ions have a high tendency to absorb on the surface of $CsPbBr_3$ due to the intrinsic property of $CsPbBr_3$. The absorption of Cs^+ ions leads to positive charges at the surface, and then Br^- is dragged around the surface by electrostatic interaction. These two layers of Cs^+ and Br^- ions form the EDL, and the first Cs^+ ions are the potential determining ions. The EDL can move with the inner NCs in water, and there is a shear plane between the EDL and solution. ζ potential is just the potential at shear plane (Fig. S9). The large ζ potential of > 80 mV of w-$CsPbBr_3$ NCs guarantees their perfect dispersion in water. More importantly, the large ζ potential can provide a high energy barrier so that the Cs^+ and Br^- ions in the w-$CsPbBr_3$ NCs will not penetrate through the EDL and leach into water (even though the concentration of CsBr is much lower than its solubility (1243 g L^{-1} at 25 °C)). Furthermore, the Cs^+ ion layer on the surface of w-$CsPbBr_3$ NCs can, in turn, improve the stability of $[PbBr_6]^{4-}$ framework, as demonstrated in Fig. 4. Therefore, w-$CsPbBr_3$ NCs can maintain high stability in water. However, if the freshly prepared w-$CsPbBr_3$ NCs were centrifuged and re-dispersed in pure water, the EDL on the surface of w-$CsPbBr_3$ NCs will be destroyed. As a result, complete quenching of the PL emission could be observed within 24 h.

3.3 Electrochemical Performance of $CsPbBr_3$ NCs

Colloidal NCs have emerged as promising materials for electrocatalytic applications due to the ability to tailor their properties through size modulation [54, 55]. However, because of the unstable and catalytically inert property of $CsPbBr_3$, it has been commonly used as either a co-catalyst or a light capture agent during the catalytic reactions [19]. Here, for the first time, we have successfully prepared ultra-water-stable $CsPbBr_3$ NCs and demonstrated their applications in electrocatalysis (Fig. 5a). The as-prepared w-$CsPbBr_3$ NCs were measured as electrocatalysts for the CO_2 RR in an H-cell using CO_2-saturated 0.1 M $KHCO_3$ as the electrolyte. The electrocatalytic reduction products were further confirmed by both gas chromatography (GC) and ^1H nuclear magnetic resonance (NMR). Figure 5b showed the faradaic efficiencies (FEs) for the w-$CsPbBr_3$ NCs from − 0.7 to − 1.2 V versus reversible hydrogen electrode (RHE). The main products of the catalyst were H_2, CO, and CH_4. At − 0.7 V, H_2 was more than 70%, which indicated that the hydrogen evolution reaction should be dominant compared to the CO_2 RR at this potential. From − 0.8 V, the CO_2 RR mainly generated both CO and CH_4; at − 1.1 V, the reaction yielded mostly CH_4 (32%), and CO (40%). To the best of our knowledge, this

 https://doi.org/10.1007/s40820-021-00690-8

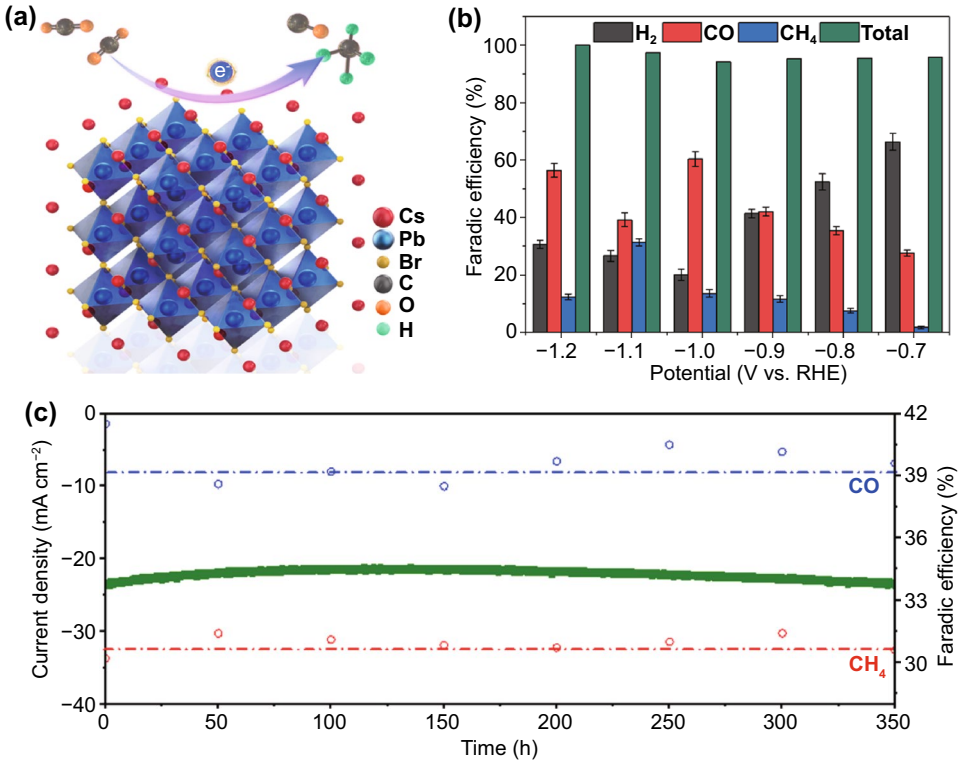

Fig. 5 **a** Schematic of the w-$CsPbBr_3$ NCs CO_2 RR; **b** Faradic efficiencies for the w-$CsPbBr_3$ NCs CO_2 RR; **c** chronopotentiometry curve (long-term stability) of w-$CsPbBr_3$ NCs in 0.1 M $KHCO_3$ for 350 h

result is the first report so far for the LHP NCs electrochemical CO_2 RR. It also showed that our catalysts did not favour the production of methanol (CH_3OH), which is one of the other CO_2 hydrogenation products. Although many transition metals have the potential to produce both methane and methanol, the ionophilicity of the surface, as measured by the Oads binding energy, plays a critical role in determining the selectivity between these two products. Additionally, the catalyst also showed ultrahigh catalytic stability for CO_2 RR with at least 350 h of long-term running for chronoamperometry (CA), as shown in Fig. 5c. Moreover, the crystal structure of the w-$CsPbBr_3$ NCs after reaction, as well as its statistic current long-term stability had also been characterized, as shown in Fig. S10. The results further confirmed the ultrahigh catalytic stability of the w-$CsPbBr_3$ NCs. For comparison, the catalytic performance of w-$CsPbBr_3$ NCs has also been carried out. The results revealed that its reaction yield of CH_4 (11%), and CO (19%) at − 1.1 V was much lower than that of w-$CsPbBr_3$ NCs (Fig. S11a). Moreover, a 34% deduction of the current density for h-$CsPbBr_3$ has been observed after 20 h (Fig. S11b). While, the current density for w-$CsPbBr_3$ can preserve about 97% of its initial value after 20 h (Fig. 5c), which suggested much higher catalytic stability of w-$CsPbBr_3$ than that of h-$CsPbBr_3$.

Further theory calculations were carried out to investigate the active site and the reaction mechanism of this reaction. Generally, the appropriate bonding energy between CO_2 molecular and active sites is necessary for the CO_2 reduction. Our theoretical results in Fig. S12 suggest that the formation of Cs–O bond is preferred to Cs–C bond. In this regard, the Cs cannot be the active site in the $CsPbBr_3$ NCs-based electrochemical CO_2 reduction reaction. However, once we choose the Pb atom as the active site, the formation of Pb–C chemical bond is favourable, as a result, the CO_2 can be reduced to CO and CH_4 (Fig. 6). These results indicate that the catalytic center should be the Pb atoms in the perovskite structure., the C–C coupling pathway between two C1 species into one C2 product was substantially inhibited, leading to a dramatic enhancement of the CH_4 formation (*i.e.*, the deepest C1 product).

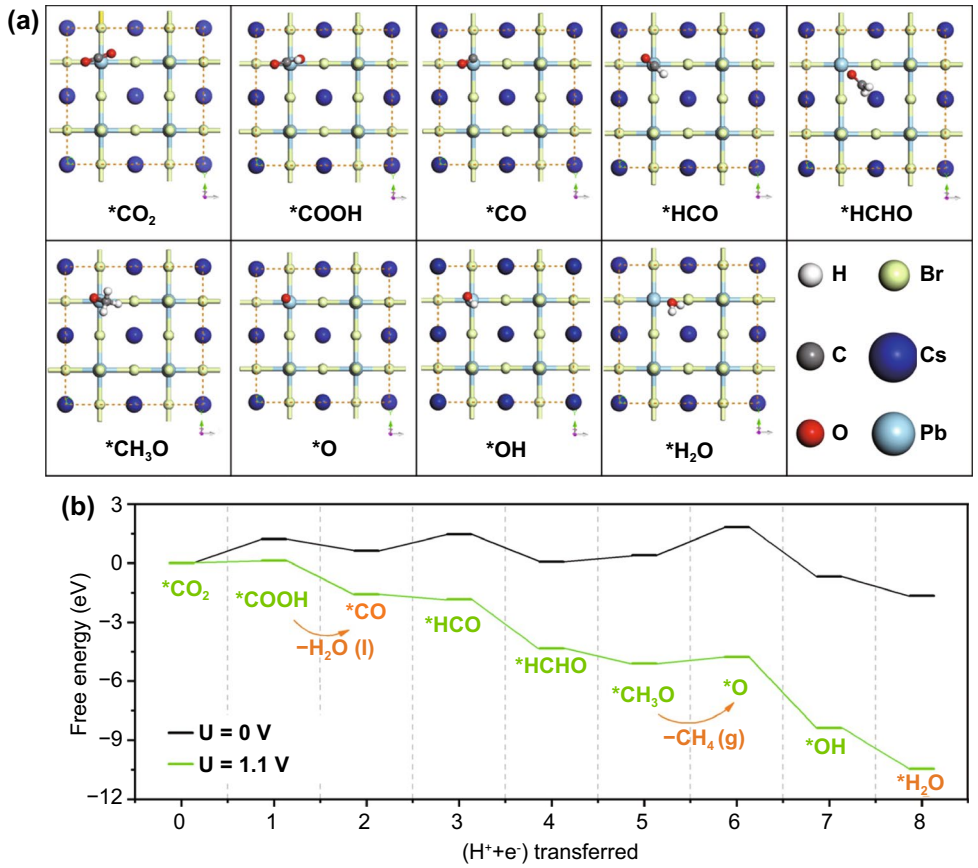

Fig. 6 Formation energy of intermediates. **a** Binding site configurations for the $CsPbBr_3$ catalysts (**b**) Energy profiles of all intermediates toward CO and CH_4. Intermediates for all the binding sites on the Pb sites are calculated and then averaged. The energy profiles are corrected to − 0.0 V and − 1.1 V vs. RHE according to the computational hydrogen electrode

4 Conclusions

In summary, water-dispersible $CsPbBr_3$ NCs with ultra-stability were successfully prepared through a Pb-poor hot-injection method combined with a well-designed purification process. The as-prepared water-dispersible $CsPbBr_3$ NCs exhibited a higher PLQY (91%) and lower defect density than the traditional hexane-dispersibility $CsPbBr_3$ NCs. Interestingly, the water-dispersible $CsPbBr_3$ NCs showed ultra-stability of 200 days with only a ~ 20% decline in the initial PL intensity. CsBr salt can passivate the surface defects induced by a loss of OLA^+ and Br^- ions, and maintain the stability of the $CsPbBr_3$ NCs structure in water. Finally, for the first time, $CsPbBr_3$ NCs showed high electrocatalytic activity and stability (> 350 h) for the CO_2 reduction reaction, providing high generation values of CH_4 (32%) and CO (40%). This work not only provides an effective method for the synthesis of water-dispersible perovskite NCs, but also shows excellent potential for their application in electrocatalysis.

Acknowledgements This research was supported by the National Natural Science Foundation of China (Nos. 11674258, 51602305, 51702219, 61975134, 11904250), Guangdong Basic and Applied Basic Research Foundation (2020B1515020051), the Science and Technology Innovation Commission of Shenzhen (JCYJ20180305125345378), and Shenzhen Nanshan District Pilotage Team Program (LHTD20170006). Partial support from The Institute For Lasers, Photonics and Biophotonics at The University at Buffalo is also acknowledged. T.Z. and I.Z. were supported by the U.S. DOE, Office of Science BES, Award No. DE-SC0004890.

Supplementary Information The online version contains supplementary material available at https://doi.org/10.1007/s40820-021-00690-8.

References

1. R. Angamuthu, P. Byers, M. Lutz, A.L. Spek, E. Bouwman, Electrocatalytic CO_2 conversion to oxalate by a copper complex. Science **327**, 313–315 (2010). https://doi.org/10.1126/science.1177981
2. J. Medina-Ramos, J.L. DiMeglio, J. Rosenthal, Efficient reduction of CO_2 to CO with high current density using in situ or ex situ prepared Bi-based materials. J. Am. Chem. Soc. **136**, 8361–8367 (2014). https://doi.org/10.1021/ja501923g
3. K. Qi, Y. Zhang, J. Li, C. Charmette, M. Ramonda et al., Enhancing the CO_2-to-CO conversion from 2D silver nanoprisms via superstructure assembly. ACS Nano **15**, 7682–7693 (2021). https://doi.org/10.1021/acsnano.1c01281
4. M. Asadi, K. Kim, C. Liu, A.V. Addepalli, P. Abbasi et al., Nanostructured transition metal dichalcogenide electrocatalysts for CO_2 reduction in ionic liquid. Science **353**, 467–470 (2016). https://doi.org/10.1126/science.aaf4767
5. X. Zhang, Z. Wu, X. Zhang, L. Li, Y. Li et al., Highly selective and active CO_2 reduction electrocatalysts based on cobalt phthalocyanine/carbon nanotube hybrid structures. Nat. Commun. **8**, 14675 (2017). https://doi.org/10.1038/ncomms14675
6. C. Chen, J.F.K. Kotyk, S.W. Sheehan, Progress toward commercial application of electrochemical carbon dioxide reduction. Chem **4**, 2571–2586 (2018). https://doi.org/10.1016/j.chempr.2018.08.019
7. A. Kojima, K. Teshima, Y. Shirai, T. Miyasaka, Organometal halide perovskites as visible-light sensitizers for photovoltaic cells. J. Am. Chem. Soc. **131**, 6050–6051 (2009). https://doi.org/10.1021/ja809598r
8. Q.A. Akkerman, G. Rainò, M.V. Kovalenko, L. Manna, Genesis, challenges and opportunities for colloidal lead halide perovskite nanocrystals. Nat. Mater. **17**, 394–405 (2018). https://doi.org/10.1038/s41563-018-0018-4
9. J.-P. Correa-Baena, M. Saliba, T. Buonassisi, M. Grätzel, A. Abate et al., Promises and challenges of perovskite solar cells. Science **358**, 739–744 (2017). https://doi.org/10.1126/science.aam6323
10. Q. Dong, Y. Fang, Y. Shao, P. Mulligan, J. Qiu et al., Electron-hole diffusion lengths >175 μm in solution-grown $CH_3NH_3PbI_3$ single crystals. Science **347**, 967–970 (2015). https://doi.org/10.1126/science.aaa5760
11. Y. Zhang, C.-K. Lim, Z. Dai, G. Yu, J.W. Haus et al., Photonics and optoelectronics using nano-structured hybrid perovskite media and their optical cavities. Phys. Rep. **795**, 1–51 (2019). https://doi.org/10.1016/j.physrep.2019.01.005
12. Y. Wang, M.I. Dar, L.K. Ono, T. Zhang, M. Kan et al., Thermodynamically stabilized β-$CsPbI_3$–based perovskite solar cells with efficiencies >18%. Science **365**, 591–595 (2019). https://doi.org/10.1126/science.aav8680
13. K. Chen, Q. Zhong, W. Chen, B. Sang, Y. Wang et al., Short-chain ligand-passivated stable α-$CsPbI_3$ quantum dot for all-inorganic perovskite solar cells. Adv. Funct. Mater. **29**, 1900991 (2019). https://doi.org/10.1002/adfm.201900991
14. K. Lin, J. Xing, L.N. Quan, F.P.G. de Arquer, X. Gong et al., Perovskite light-emitting diodes with external quantum efficiency exceeding 20 per cent. Nature **562**, 245–248 (2018). https://doi.org/10.1038/s41586-018-0575-3
15. K. Chen, W. Jin, Y. Zhang, T. Yang, P. Reiss et al., High efficiency mesoscopic solar cells using $CsPbI_3$ perovskite quantum dots enabled by chemical interface engineering. J. Am. Chem. Soc. **142**, 3775–3783 (2020). https://doi.org/10.1021/jacs.9b10700
16. C.-T. Wang, K. Chen, P. Xu, F. Yeung, H.-S. Kwok et al., Fully chiral light emission from $CsPbX_3$ perovskite nanocrystals enabled by cholesteric superstructure stacks. Adv. Funct. Mater. **29**, 1903155 (2019). https://doi.org/10.1002/adfm.201903155
17. Z. Chen, Y. Hu, J. Wang, Q. Shen, Y. Zhang et al., Boosting photocatalytic CO_2 reduction on CsPbBr 3 perovskite nanocrystals by immobilizing metal complexes. Chem. Mater. **32**, 1517–1525 (2020). https://doi.org/10.1021/acs.chemmater.9b04582
18. J. Wang, J. Wang, N. Li, X. Du, J. Ma et al., Direct Z-scheme 0D/2D heterojunction of $CsPbBr_3$ quantum dots/Bi_2WO_6 nanosheets for efficient photocatalytic CO_2 reduction. ACS Appl. Mater. Interfaces **12**, 31477–31485 (2020). https://doi.org/10.1021/acsami.0c08152
19. Y.-F. Xu, M.-Z. Yang, B.-X. Chen, X.-D. Wang, H.-Y. Chen et al., A $CsPbBr_3$ perovskite quantum dot/graphene oxide composite for photocatalytic CO_2 reduction. J. Am. Chem. Soc. **139**, 5660–5663 (2017). https://doi.org/10.1021/jacs.7b00489
20. B. Saparov, D.B. Mitzi, Organic–inorganic perovskites: structural versatility for functional materials design. Chem. Rev. **116**, 4558–4596 (2016). https://doi.org/10.1021/acs.chemrev.5b00715
21. G. Li, K. Chen, Y. Cui, Y. Zhang, Y. Tian et al., Stability of perovskite light sources: status and challenges. Adv. Opt. Mater. **8**, 1902012 (2020). https://doi.org/10.1002/adom.201902012
22. K. Chen, C. Wang, Z. Peng, K. Qi, Z. Guo et al., The chemistry of colloidal semiconductor nanocrystals: from metal-chalcogenides to emerging perovskite. Coord. Chem. Rev. **418**, 213333 (2020). https://doi.org/10.1016/j.ccr.2020.213333
23. W. Lv, L. Li, M. Xu, J. Hong, X. Tang et al., Improving the stability of metal halide perovskite quantum dots by

encapsulation. Adv. Mater. **31**, 1900682 (2019). https://doi.org/10.1002/adma.201900682

24. Z. Li, Q. Hu, Z. Tan, Y. Yang, M. Leng et al., Aqueous synthesis of lead halide perovskite nanocrystals with high water stability and bright photoluminescence. ACS Appl. Mater. Interfaces **10**, 43915–43922 (2018). https://doi.org/10.1021/acsami.8b16471
25. F. Palazon, Q.A. Akkerman, M. Prato, L. Manna, X-ray lithography on perovskite nanocrystals films: from patterning with anion-exchange reactions to enhanced stability in air and water. ACS Nano **10**, 1224–1230 (2016). https://doi.org/10.1021/acsnano.5b06536
26. X. Zhang, X. Bai, H. Wu, X. Zhang, C. Sun et al., Water-assisted size and shape control of $CsPbBr_3$ perovskite nanocrystals. Angew. Chem. Int. Ed. **57**, 3337–3342 (2018). https://doi.org/10.1002/anie.201710869
27. H. Huang, B. Chen, Z. Wang, T.F. Hung, A.S. Susha et al., Water resistant $CsPbX_3$ nanocrystals coated with polyhedral oligomeric silsesquioxane and their use as solid state luminophores in all-perovskite white light-emitting devices. Chem. Sci. **7**, 5699–5703 (2016). https://doi.org/10.1039/c6sc01758d
28. L. Wu, H. Hu, Y. Xu, S. Jiang, M. Chen et al., From nonluminescent Cs_4PbX_6 (X = Cl, Br, I) nanocrystals to highly luminescent $CsPbX_3$ nanocrystals: water-triggered transformation through a CsX-stripping mechanism. Nano Lett. **17**, 5799–5804 (2017). https://doi.org/10.1021/acs.nanolett.7b02896
29. Y. Wang, L. Varadi, A. Trinchi, J. Shen, Y. Zhu et al., Spray-assisted coil-globule transition for scalable preparation of water-resistant $CsPbBr_3$@PMMA perovskite nanospheres with application in live cell imaging. Small **14**, 1803156 (2018). https://doi.org/10.1002/smll.201803156
30. C. Geng, S. Xu, H. Zhong, A.L. Rogach, W. Bi, Aqueous synthesis of methylammonium lead halide perovskite nanocrystals. Angew. Chem. Int. Ed. **57**, 9650–9654 (2018). https://doi.org/10.1002/anie.201802670
31. M. Crespo-Quesada, L.M. Pazos-Outon, J. Warnan, M.F. Kuehnel, R.H. Friend et al., Metal-encapsulated organolead halide perovskite photocathode for solar-driven hydrogen evolution in water. Nat. Commun. **7**, 12555 (2016). https://doi.org/10.1038/ncomms12555
32. Q. Zhong, M. Cao, H. Hu, D. Yang, M. Chen et al., One-pot synthesis of highly stable $CsPbBr_3$@SiO_2 core-shell nanoparticles. ACS Nano **12**, 8579–8587 (2018). https://doi.org/10.1021/acsnano.8b04209
33. G. Li, Z.-K. Tan, D. Di, M.L. Lai, L. Jiang et al., Efficient light-emitting diodes based on nanocrystalline perovskite in a dielectric polymer matrix. Nano Lett. **15**, 2640–2644 (2015). https://doi.org/10.1021/acs.nanolett.5b00235
34. Z.-J. Li, E. Hofman, J. Li, A.H. Davis, C.-H. Tung et al., Photoelectrochemically active and environmentally stable $CsPbBr_3/TiO_2$ core/shell nanocrystals. Adv. Funct. Mater. **28**, 1704288 (2018). https://doi.org/10.1002/adfm.201704288
35. A. Jana, K.S. Kim, Water-stable, fluorescent organic−inorganic hybrid and fully inorganic perovskites. ACS Energy Lett. **3**, 2120–2126 (2018). https://doi.org/10.1021/acsenergylett.8b01394
36. A. Jana, Q. Ba, K.S. Kim, Compositional and dimensional control of 2D and quasi-2D lead halide perovskites in water. Adv. Funct. Mater. **29**, 1900966 (2019). https://doi.org/10.1002/adfm.201900966
37. Q. Ba, A. Jana, L. Wang, K.S. Kim, Dual emission of water-stable 2D organic–inorganic halide perovskites with Mn(II) dopant. Adv. Funct. Mater. **29**, 1904768 (2019). https://doi.org/10.1002/adfm.201904768
38. M. Xie, H. Liu, F. Chun, W. Deng, C. Luo et al., Aqueous phase exfoliating quasi-2D $CsPbBr_3$ nanosheets with ultrahigh intrinsic water stability. Small **15**, 1901994 (2019). https://doi.org/10.1002/smll.201901994
39. Y. Dong, T. Qiao, D. Kim, D. Parobek, D. Rossi et al., Precise control of quantum confinement in cesium lead halide perovskite quantum dots via thermodynamic equilibrium. Nano Lett. **18**, 3716–3722 (2018). https://doi.org/10.1021/acs.nanolett.8b00861
40. S. Sun, D. Yuan, Y. Xu, A. Wang, Z. Deng, Ligand-mediated synthesis of shape-controlled cesium lead halide perovskite nanocrystals via reprecipitation process at room temperature. ACS Nano **10**, 3648–3657 (2016). https://doi.org/10.1021/acsnano.5b08193
41. P.E. Blöchl, Projector augmented-wave method. Phys. Rev. B **50**, 17953–17979 (1994). https://doi.org/10.1103/PhysRevB.50.17953
42. G. Kresse, J. Furthmüller, Efficient iterative schemes for ab initio total-energy calculations using a plane-wave basis set. Phys. Rev. B **54**, 11169–11186 (1996). https://doi.org/10.1103/PhysRevB.54.11169
43. J.P. Perdew, K. Burke, M. Ernzerhof, Generalized gradient approximation made simple. Phys. Rev. Lett. **77**, 3865–3868 (1996). https://doi.org/10.1103/PhysRevLett.77.3865
44. S. Grimme, J. Antony, S. Ehrlich, H. Krieg, A consistent and accurate ab initio parametrization of density functional dispersion correction (DFT-D) for the 94 elements H-Pu. J. Chem. Phys. **132**, 154104 (2010). https://doi.org/10.1063/1.3382344
45. A. Swarnkar, A.R. Marshall, E.M. Sanehira, B.D. Chernomordik, D.T. Moore et al., Quantum dot–induced phase stabilization of α-$CsPbI_3$ perovskite for high-efficiency photovoltaics. Science **354**, 92–95 (2016). https://doi.org/10.1126/science.aag2700
46. L. Wu, K. Chen, W. Huang, Z. Lin, J. Zhao et al., Perovskite $CsPbX_3$: a promising nonlinear optical material and its applications for ambient all-optical switching with enhanced stability. Adv. Opt. Mater. **6**, 1800400 (2018). https://doi.org/10.1002/adom.201800400
47. K. Chen, Y. Wang, J. Liu, J. Kang, Y. Ge et al., In situ preparation of a $CsPbBr_3$/black phosphorus heterostructure with an optimized interface and photodetector application. Nanoscale **11**, 16852–16859 (2019). https://doi.org/10.1039/c9nr06488e
48. Y. Wang, K. Chen, H. Hao, G. Yu, B. Zeng et al., Engineering ultrafast charge transfer in a bismuthene/perovskite nanohybrid. Nanoscale **11**, 2637–2643 (2019). https://doi.org/10.1039/c9nr00058e

 https://doi.org/10.1007/s40820-021-00690-8

49. J. Shamsi, A.S. Urban, M. Imran, L. De Trizio, L. Manna, Metal halide perovskite nanocrystals: synthesis, post-synthesis modifications, and their optical properties. Chem. Rev. **119**, 3296–3348 (2019). https://doi.org/10.1021/acs.chemrev.8b00644
50. S. Yang, S. Chen, E. Mosconi, Y. Fang, X. Xiao et al., Stabilizing halide perovskite surfaces for solar cell operation with wide-bandgap lead oxysalts. Science **365**, 473–478 (2019). https://doi.org/10.1126/science.aax3294
51. J.K. Sun, S. Huang, X.Z. Liu, Q. Xu, Q.H. Zhang et al., Polar solvent induced lattice distortion of cubic $CsPbI_3$ nanocubes and hierarchical self-assembly into orthorhombic single-crystalline nanowires. J. Am. Chem. Soc. **140**, 11705–11715 (2018). https://doi.org/10.1021/jacs.8b05949
52. D. Jain, S. Chaube, P. Khullar, S.G. Srinivasan, B. Rai, Bulk and surface DFT investigations of inorganic halide perovskites screened using machine learning and materials property databases. Phys. Chem. Chem. Phys. **21**, 19423–19436 (2019). https://doi.org/10.1039/c9cp03240a
53. Y. Liang, N. Hilal, P. Langston, V. Starov, Interaction forces between colloidal particles in liquid: theory and experiment. Adv. Colloid Interface Sci. **134–135**, 151–166 (2007). https://doi.org/10.1016/j.cis.2007.04.003
54. H. Zhang, M. Jin, Y. Xia, Enhancing the catalytic and electrocatalytic properties of Pt-based catalysts by forming bimetallic nanocrystals with Pd. Chem. Soc. Rev. **41**, 8035–8049 (2012). https://doi.org/10.1039/C2CS35173K
55. Y.-J. Wang, W. Long, L. Wang, R. Yuan, A. Ignaszak et al., Unlocking the door to highly active ORR catalysts for PEMFC applications: polyhedron-engineered Pt-based nanocrystals. Energy Environ. Sci. **11**, 258–275 (2018). https://doi.org/10.1039/C7EE02444D